Shear Instabilities and Stratified Turbulence in an Estuarine Fluid Mud

Junbiao Tu, [a] Daidu Fan,[a*] Feixiang Sun, [a] Alexis Kaminski, [b] William Smyth[c*]

[a] *State Key Laboratory of Marine Geology, Tongji University, Shanghai, China*

[b] *Department of Mechanical Engineering, University of California, Berkeley, Berkeley, California, USA*

[c] *College of Oceanic and Atmospheric Sciences, Oregon State University, Corvallis, Oregon, USA*

**Corresponding authors*:

D. Fan, ddfan@tongji.edu.cn;

W. Smyth, bill.smyth@oregonstate.edu

ABSTRACT

This study presents field observations of fluid mud and the flow instabilities that result from the interaction between mud-induced density stratification and current shear. Data collected by ship-borne and bottom-mounted instruments in a hyperturbid estuarine tidal channel reveal the details of turbulent sheared layers in the fluid mud which persists throughout the tidal cycle. Shear instabilities form during periods of intense shear and strong mud-induced stratification, particularly with gradient Richardson number smaller than or fluctuating around the critical value of 0.25. Turbulent mixing plays a significant role in the vertical entrainment of fine sediment over the tidal cycle.

The vertical extent of the billows identified seen in the acoustic images is the basis for two useful parameterizations. First, the aspect ratio (billow height/wavelength) is indicative of the initial Richardson number that characterizes the shear flow from which the billows grew. Second, we describe a scaling for the turbulent dissipation rate ε that holds for both observed and simulated K-H billows. Estimates for the present observations imply, however, that billows growing on a lutocline obey an altered scaling whose origin remains to be explained.

1. Introduction

Turbidity maxima with high concentrations of suspended sediment are ubiquitous in estuaries due to a combination of hydrodynamic and sediment dynamic processes (*Burchard et al.*, 2018, and references therein). In hyperturbid estuaries, the near-bottom layer of high-concentration, fine (particle size < 63 um) suspended sediment is generally referred to as fluid mud (FM, *McAnally et al.*, 2007). The motion of estuarine FM is modulated by the tidal cycle (*Bruens et al.*, 2012), with resuspension and entrainment during phases of high flow velocity and settling in slower flow. Current shear, induced by bottom friction, provides an energy source for shear instability, while stratification induced by concentrated sediment (e.g., *Becker et al.*, 2018; *Tu et al.*, 2019) tends to stabilize the flow. Although this process has been reproduced in the laboratory (*Scarlatos and Mehta*, 1993), field observations of shear instability in FM remain scarce. In the turbid Ems Estuary, *Held et al.* (2013, 2019) observed cusped waves suggestive of asymmetric Holmboe instability (*Carpenter et al.*, 2007). *Tu et al*. (2020) observed symmetric Kelvin-Helmholtz (K-H) billows on an estuarine lutocline for the first time using echosounder images. They showed that the instabilities might play an important role in sediment entrainment and mixing across the lutocline. However, detailed measurements of FM and/or lutoclines linking shear instabilities and turbulent mixing are scarce due to technical challenges (*Becker et al.*, 2018; *Sottolichio et al.*, 2011). In this paper we analyze measurements, including the turbulent kinetic energy dissipation rate, from the Changjiang estuary through which the Yangtze river empties into the East China Sea.

K-H billows have been well observed in the laboratory (e.g., *Thorpe*, 1973). In the ocean, observations were successfully carried out photographically (*Woods*, 1969), acoustically (e.g., *Moum et al.*, 2003) and using finely-spaced temperature sensor arrays (e.g., *Hebert et al.,* 1992*; Van Haren and Gostiaux,* 2010). Echosounder images have been used to identify shear instabilities in salt-wedge estuaries by *Geyer et al. (2010)* and *Tedford et al. (2009)*. K-H instability is also observed throughout the Earth's atmosphere (*Lee,* 1997; *Fukao et al.,* 2011; *Fritts et al.,* 2014), where they often form banded clouds.

These observations have shown that billows can be interpreted using the gradient Richardson number $Ri = N^2/S^2$, where $N^2 = -\frac{g}{\rho}\frac{\partial \rho}{\partial z}$ is the squared buoyancy frequency and $S^2 = (\frac{\partial u}{\partial z})^2 + (\frac{\partial v}{\partial z})^2$ is the squared vertical shear of the mean horizontal current. The coordinate z points vertically upward, opposite to the gravitational acceleration g; ρ is the density (determined in this case by salinity, temperature, and suspended sediment concentration), and u and v are horizontal velocity components to be specified later.

In the limit of inviscid, non-diffusive, steady flow, K-H instability may arise if the shear is sufficiently strong, relative to stratification, that the minimum value of $Ri < 0.25$ (*Miles*, 1961; *Howard*, 1961). Observations of fully turbulent KH billows also suggest a critical Ri of 0.25 (e.g., *Chang et al.*, 2016). However, under-resolution might cause the Ri estimates to be too high compared to the canonical value of 0.25 (e.g., *Moum et al.*, 2003). In forced shear flows, Ri can fluctuate around 0.25 due to the repetitive growing, breaking, and decaying of the billows (e.g., *Tu et al.*, 2020), a state often referred to as marginal instability (e.g., *Smyth et al.*, 2019; *Smyth*, 2020).

Shear instability is a major mechanism of turbulent mixing in oceanic stratified flow (*Smyth and Moum*, 2012). Observations in the ocean interior (*Chang et al.*, 2016; *Moum et al.*, 2003; *Seim and Gregg*, 1994) and in estuarine flows (*Geyer et al.*, 2010) reveal elevated turbulence levels coinciding with the billows that result from the instability. Estimation of turbulent quantities such as the turbulent kinetic energy dissipation rate is challenging due to the need to measure fluctuating quantities accurately on fine spatiotemporal scales (*Caulfield*, 2021), often from a moving platform. Thus, it is useful to parameterize mixing using readily measured quantities (e.g., *Klymak and Legg*, 2010). Here we discuss a parameterization based on the billow height as registered by an echosounder.

We present observations of shear instabilities within an estuarine FM as it interacts with the oscillating tidal flow. We use measurements from a shipboard echosounder and CTD-OBS casts (conductivity, temperature, depth, and optical backscatter sensor), as well as water samples. A bottom mounted tripod system was added in order to measure the tidal flow using an ADCP (acoustic Doppler current profiler) and near-bed turbulence via high-resolution acoustic pulse-coherent Doppler velocity profiles. Acoustic imagery of the billows is presented, together with analyses of their properties and formation mechanisms. The billows' aspect ratio can be used to infer the initial flow condition prior to billows' formation. The echograms are further used to quantify the turbulent mixing, which may explain the exchange of the FM with the overlying, less turbid water. We discuss the possibility of a turbulent mixing parameterization based on readily-obtained quantities: the density profile and the vertical scale of the billows as shown in the acoustic images.

This study extends the previous work of *Tu et al*. (2020, hereafter T20). In that work, we analyzed observations from the Jiaojiang estuary, examining hydrographic variations (e.g., tidal current, salinity, SSC, etc.) during a 25-hr tidal cycle, echosounder images showing internal wave and instabilities, and velocity and density profiles synchronous with typical billow trains. Here, using new observations made in the Changjiang estuary, we repeat those analyses and in addition measure the turbulence associated with the shear instabilities. We also combine previous and present observations with DNS results and propose parameterizations for the TKE dissipation rate and the initial Richardson number based on the vertical extent of the observed billows.

In section 2 we describe observational details and analysis methods. Results are described and discussed in the context of existing knowledge and research questions in sections 3-6. We focus in turn on variations over the tidal cycle (section 3), on the physical mechanisms for individual instability events (section 4), on the turbulent mixing that results (section 5), and on the applicability of ε parameterization to the lutocline case (section 6). While shear instability is the underlying mechanism, we find significant differences between these observations and instances of shear instability in other geophysical regimes. In section 7 we summarize the major findings and suggest future work.

2. Data and methods

The North Branch of the Changjiang estuary (the lowest reach of the Yangtze River, Figure 1) in SE China is a shallow, tidally-dominated distributary with mean water depth up to ~ 8 m (*Dai et al.*, 2016). The sea bed is mainly mud with mean grain size ~ 8 µm. Approximately 25 hours of data were measured starting from 10:00, 2 October 2018 (local time) in the main tidal channel of the North Branch. The mean water depth was ~ 6m during the observational period.

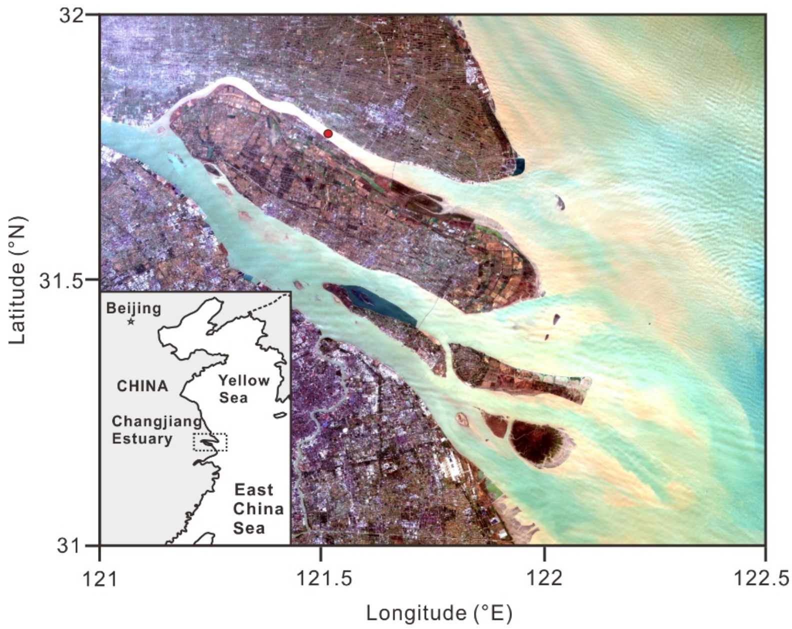

Fig. 1. Study area, satellite image courtesy of USGS. The red circle shows the location of observational site.

A dual frequency echosounder (24/200 kHz) was deployed on the vessel side at 0.6 m below the sea surface to measure water depth and collect acoustic images. Vertical profiles of salinity, temperature, and turbidity were measured every 0.5 hr using a CTD with a built-in OBS 3+, sampling at 2 Hz. The OBS outputs were converted to suspended sediment concentration (SSC) using the filtered water samples. The water-sediment mixture density was determined combining SSC, salinity, and temperature. The buoyancy frequency was calculated using this density, which was dominated by high SSC. The determination of SSC and density is described in Text S1 in the supplemental material. The salinity and temperature measured by CTD are used to calculate seawater density ρ_{sw}. The density of the water-sediment mixture is then estimated using the SSC via $\rho = \rho_{sw}\left[1-\left(\frac{SSC}{\rho_s}\right)\right] + SSC$ (*Wright et al.*, 1986), where ρ_s= 2650 kg m^{-3} is the sediment density.

Concurrent near-bed observations were carried out using a bottom mounted tripod. A downward-looking 2 MHz Aquadopp HR profiler (referred to as ADP hereafter) was set to burst mode, collecting 1024 profiles at 300-s intervals with a sampling rate of 4 Hz, so that the burst duration was 256s. The ADP collected velocity profiles between 0.04-0.92 mab (meters above consolidated bed) with a vertical bin size of 0.04 m. An up-looking acoustic Doppler current profiler (ADCP) was deployed at 1.9 meters above consolidated bed (mab) sampling at 0.5 Hz and recording an average over 180s with a vertical resolution of 0.5m. A 2-D electro-magnetic current meter (EMCM) was deployed at 1 mab sampling at 1 Hz and recording horizontal velocity components averaged over 30s. More details of the instrumentation are summarized in Table 1.

Table 1. Summary of Instrumentation

Instrument	Nominal Sampling range (mab)	Bin size (m)	Sampling Interval (s)	Range	Accuracy	Looking direction
Aquadopp	0.04-0.96	0.04	1/4	0-0.84 m s^{-1}	± 0.5%	Downward
EMCM	1	-	30	0-5 m s^{-1}	± 2%	Downward
ADCP	1.9-	0.5	180	0-5 m s^{-1}	± 0.3%	Upward
Echosounder	Water column	0. 01	1/16	-	-	Downward
CTD-OBS 3+	Water column	–	1/2	Con.: 0-90 mS cm^{-1} Temp.: -5-35 ℃ OBS: 0-4000 NTU	± 0.05% 0.002 ℃ ± 2%	-

Observations by ADP with a pulse-to-pulse correlation c<50 and/or backscatter amplitude a<30 are excluded. If the number of excluded values exceeds 50% of the total data points in a segment, the segment is rejected. The ADP data can suffer from signal attenuation under high sediment concentration due to its high operating frequency and is therefore quality controlled (QC-ed) prior to further analysis. More details of quality control of the ADP data are given in Text S2 in the supplemental material. The QC-ed ADP along beam velocities were used to determine the turbulent kinetic energy dissipation rate, ε, in the bottom layer 0.04-0.92 mab, using the structure function method (see Appendix A for details). The velocity records are rotated into streamwise (u, positive upstream) and spanwise (v, positive toward the south bank) velocities. The shear production $P = -\langle u'w' \rangle \frac{\partial u}{\partial z}$, where u' and w' are streamwise and vertical velocity perturbations, was calculated independently for comparison. Estimates of P and ε roughly agree (see Appendix A), and differences are consistent with expected buoyancy effects, suggesting that the structure function method provides reliable dissipation estimates.

Interpretation of these data was aided by three-dimensional DNS (direct numerical simulations) of turbulent K-H billows. The simulations focus on a single wavelength of an infinite K-H wave train as it grows, breaks down into turbulence and ultimately dissipates. From the DNS output we estimate echo strength, billow height, and various turbulence statistics. Details are given in Appendix B.

3. Intra-tidal variations in hydrographic structure and fluid mud distribution

As indicated by velocities measured at mid-water-column (3.4 mab, Figure 2d), the durations and magnitude of flood and ebb currents are comparable. A persistent presence of FM is evident throughout the entire ~ 25-hr tidal cycle (Figure 2b). The thickness of the FM layer (defined by SSC > 10g/L, black contour, Figure 2b) varies between 1-2.5 m depending on the tidal phase. Another lutocline was observed between 0-1 mab (red contour, Figure 2b) with SSC greater than 100 g/L, suggesting that the viscosity of FM may be elevated (Mehta, 2013). However, this effect is expected to be minor as we focus on the layers with internal waves and instabilities where SSCs are mainly O (10) kg m^{-3} (See Figure a_2-f_2 and Appendix C for further discussion).

It appears that, during high flow periods (Hour 11-16 and Hour 22-28), the FM layer thickens and serves as a sediment source for the overlying water (Figure 2c). Note that during periods of flow transition (Hour 16-19 and 29-36), the upper layer water slows down and changes from flood to ebb, and velocity within FM is close to zero, suggesting that the FM was not mixing with the overlying water. Thus, the fresher water is trapped in the lower FM layer while the salty upper layer continues to flow upstream. As a consequence, reduced salinity was observed in lower water column compared to the water immediately above, especially within the FM (e.g., Hour 16-20, Figure 2a), a phenomenon frequently observed in estuarine FM environments (e.g., the Huanghe, *Wang and Wang*, 2010); the Gironde, *Sottolichio et al.*, 2011; or the Ems, *Becker et al.*, 2018). The decreased salinity might be artificial as the CTD conductivity cell could be affected by high sediment concentration (*Kineke and Sternberg*, 1995). However, experimental studies indicate this effect is negligible at low salinity (< 10 psu) (*Dai et al.*, 2011, Figure S1 in the supplemental material), as is the case in this study. Thus, we believe that the salinity reduction in the near bed region is associated with separate flow regimes within and out of FM as discussed above.

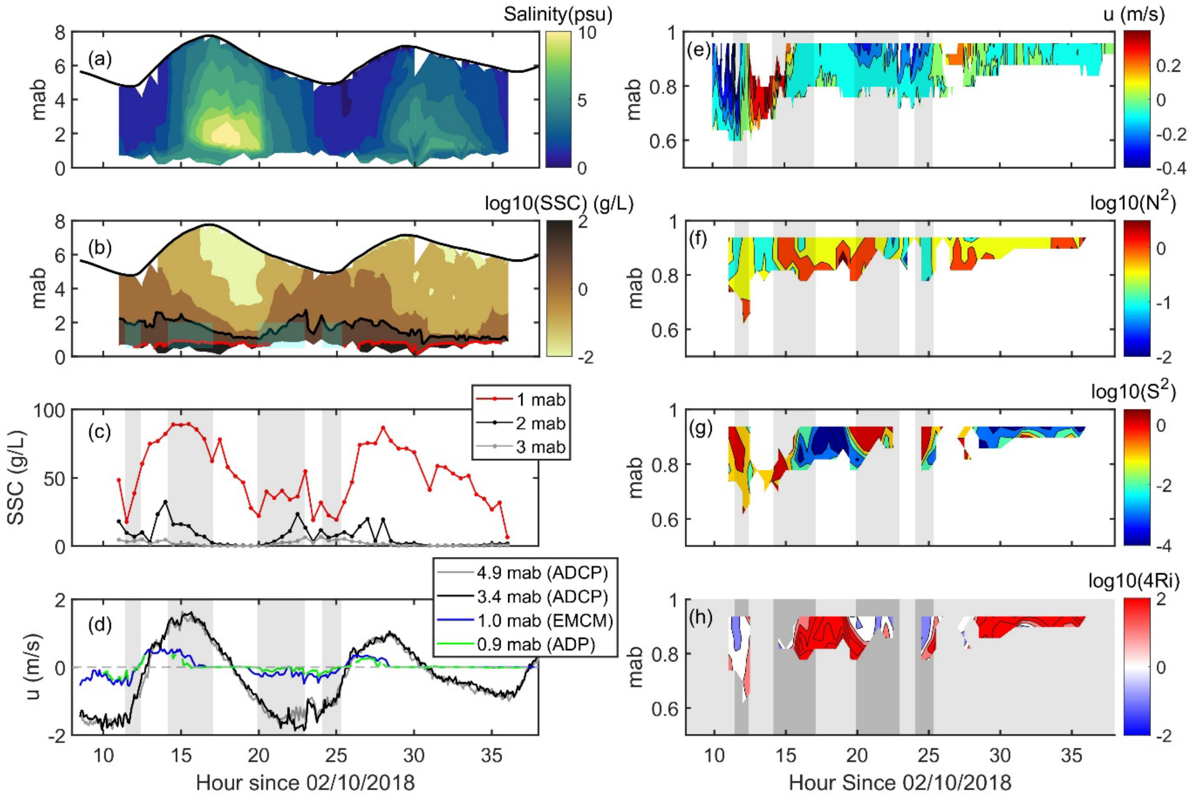

Fig. 2. Depth-time variations in (a) salinity and (b) SSC, and time series of SSC (c) and streamwise velocities (d) at different elevations. Near bed structure of (e) streamwise velocities measured by ADP, (f) buoyancy frequency squared, (g) shear squared, and (h) gradient Richardson number are also presented. Shadowed areas represent the approximate periods wherein the internal waves and billows are identified from the echosounder images.

Flow regimes within the FM layer were investigated using the near-bed ADP data. Although the nominal range of ADP was 0.04-0.96 mab, the available velocity profile range is reduced due to acoustical signal attenuation by FM (Figure 2e). The buoyancy frequency N (Figure 2f) varies approximately between 0.3-1.7 s^{-1}, indicating strong sediment stratification. Stratification is usually stronger in estuaries than in the open ocean, but these values are well above a typical value ($N = 0.3$ s^{-1}) for salt wedge estuaries (*Geyer et al.*, 2010) as well as that at a lutocline in hypertidal estuary (tidally averaged value of ~ 0.4 s^{-1} and maximum value of 0.7 s^{-1}, *Becker et al.*, 2018). The squared shear S^2 ranges from 10^{-4} to 2.5 s^{-2} (Figure 2g). Low values of Ri generally coincide with observations of instability and turbulence. The greater variation in shear compared to stratification indicates that the temporal variations in Ri (Figure 2h) are dominated by shear, i.e., low Ri values correspond primarily to strong shear, and vice versa.

Around peak flood and peak ebb, large velocity differences were observed between 1 mab and 3.4 mab (Figure 2d). Remarkable SSC differences occur between 1 and 2 mab, indicating the presence of a sharp density interface at this region (Figure 2c). The interaction between current shear and mud-induced stratification might lead to the formation of internal waves and/or billows (*Tu et al.*, 2020). Such is the case in this study as well-defined billows were identified from the echosounder image at several periods covering both flood and ebb phase (Hour 11.5-12.5; Hour 14-17; Hour 20-23; Hour 24-25.5, gray shading areas in Figure 2). These periods were also characterized by Ri below or fluctuating around 0.25 at regions below 1 mab (gray shaded areas in Figure 2h), a condition favoring shear instability. Periods with extremely high Ri values suggest reduced flow (e.g., Hour 17-19; Hour 30-32) or turbulence dampening by high SSC (e.g., Hour 32-35 when current is not weak).

4. Internal waves, instability and billows

Echosounder images often reveal wavelike structures suggestive of shear instability (Figure 3, shaded bands) in the near-bed region. No surface waves (*Trowbridge and Traykovski*, 2015) or bed forms (*Tedford et al.*, 2009) were present during the observational period.

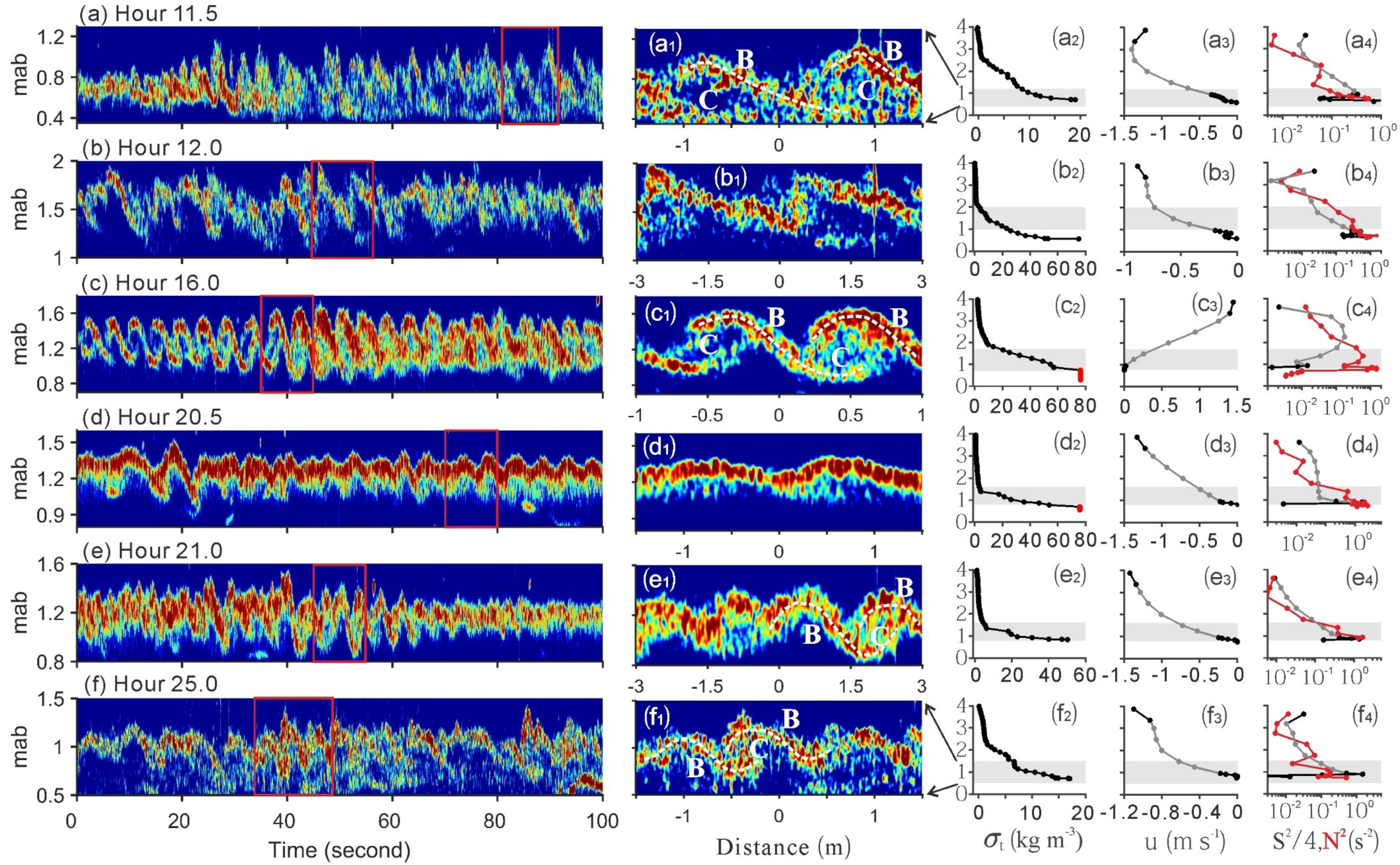
(a) Hour 11.5
(b) Hour 12.0
(c) Hour 16.0
(d) Hour 20.5
(e) Hour 21.0
(f) Hour 25.0
mab
Time (second)
Distance (m)
σ_t (kg m^{-3})
u (m s^{-1})
$S^2/4$, N^2 (s^{-2})

Fig. 3. Echosounder images and profiles of water-sediment mixture density, streamwise velocity, shear, and buoyancy frequency. Zoomed-in views for typical structures are shown in the mid-panel. For disturbances interpreted as K-H billows, braids are indicated as white dashed curves and symbol “B” and cores represented as “C”. Shaded bands show the depth range of the acoustic image at left. Gray dots indicate cubic spline interpolations using the lowest two data points from ADCP and the 3 uppermost data points from ADP. Densities of water-sediment mixture are represented by $\sigma_t = \rho$-1000. SSC values > 100 g/L (the upper limit of the measurements) were indicated by red dots. Black and red dotted lines in a_3-f_3 represent $S^2/4$ and N^2, respectively. Note that $S^2/4 > N^2$, is equivalent to Ri<1/4. Gray dots in a_3-f_3 indicate $S^2/4$ based on interpolated velocities. On the frames at the right, horizontal grey bands indicate the depth range shown in the images at left.

a. Stratification, shear, and instability

We next describe six examples of wavelike disturbances in the echogram as illustrated in Figure 3. Interpretation of these results is subject to three important caveats. First, the time dependence of the echogram represents an unknown combination of true time evolution and advection by the horizontal mean flow. Second, the incomplete velocity measurements are often interpolated through regions of interest. Third, neither density nor velocity profiles represent the initial state prior to instability growth. The latter is a challenge because the initial state is used to define the particular shear instability mechanism in theoretical, numerical and laboratory studies (e.g. *Smyth and Carpenter*, 2019). We return to this issue in section 4b.

- At Hour 11.5 (Figure 3a), the acoustic signal was enhanced, indicating the growth of wavelike disturbances and small-scale structure centered at ~ 0.7 mab. Following the growth phase, braid-core structures are visible (Figure 3a_1). Stable stratification was localized in the layer 0.4-1.2 mab, a region with significant shear as well, resulting in $Ri < 0.25$ at some depths (Figure 2h; Figure 3a_3). In the later part of the measurement, a wavelike signal emerged. The asymmetric form suggests wave steepening and resembles the distinctive S-shape identified by *Geyer et al*. (2010) and others in observations of K-H billows. We therefore interpret this event as resulting from shear instability.
- At Hour 12, billows appeared at a greater height, 1.2-2 mab (Figure 3b). Steepening is evident, with sharp cusps on both crests and troughs. Although no

direct velocity measurements are available in this region, large shear is implied by the interpolated velocities in Figure $3b_2$.

- The most beautiful, well-organized billows with clear, symmetric braid-core structures (K-H category) occur at Hour 16 at 0.8-1.6 mab (Figure 3c). This vertical range corresponds approximately to the stratified layer. Note that, although the sign of the shear is reversed in this case (Figure $3c_3$), the polarity of the billow structures remains the same, with the braids (the brightest red regions) descending in time. This is because the mean flow direction reverses with the tidal phase, i.e., the product of u and du/dz has the same sign in all cases.
- At Hour 20.5, the acoustic image suggests internal wave-like structures with no sign of steepening that would indicate instability (Figure 3d). The Ri values below 0.9 mab appear to change from a stable ($Ri > 0.25$) to an unstable regime ($Ri < 0.25$) (Figure 2h). It is interesting that the Ri values tend to decrease to values < 0.25 at the top and base of the layer containing the billows (Figure $2d_4$). Note that the lowest $S^2/4$ data point in Figure $2d_4$ is likely unreliable as the flow velocities inside this particular FM layer decay sharply toward the bottom and remains low, hence the vertical gradient vanishes. This is also true for other times with extremely large Ri values caused by small S^2 at the lowest heights approaching the (hydrodynamic) bed (i.e., u ~ 0m/s).
- At Hour 21 (Figure 3e), the wavelike features resemble K-H billows, with discernible roll-up structure. The interpolated velocity profile suggests that the shear increased while the density gradient remained comparable to Hour 20.5, resulting in decreased Ri (Figure $3e_4$).
- At Hour 25 (Figure 3f), the echosounder signal reveals a combination of overturning billows and small-scale density variations which suggest turbulent breakdown of the billows. The shear layer appears to coincide with the density interface, resulting in shear instabilities occurring at 0.6-1.2 mab.

In summary, the six examples shown in Figure 3 exhibit shear instabilities, (breaking) internal waves, and small-scale structure. The Ri values (estimated over 256s) in the regions with billows are well below 0.25 at Hour 11.5 and Hour 25. For other periods, instability coincides with near-bed Ri below or fluctuating around 0.25. These periods were also characterized by large (interpolated) current shear in the mid-upper water column. The approximated *Ri* values are found to fluctuate around or slightly above 0.25 during these periods.

b. Aspect ratio and the initial Ri

The ratio of maximum billow height to wavelength has been called the aspect ratio (e.g., *Tu et al*., 2020), and is equivalent to the steepness as defined in the original lab experiments of *Thorpe* (1973). The aspect ratio is known to be a strong function of Ri_0, the minimum gradient Richardson number that existed when the instability first began to grow (*Thorpe*, 1973). Ri_0 is difficult to define in nature but is crucial for connecting observations with the theory of idealized linear instabilities (e.g., *Miles*, 1961; *Smyth and Carpenter*, 2019), with lab experiments (e.g., *Thorpe*, 1973) and with numerical simulations (e.g., *Mashayek et al.*, 2017; *Kaminski and Smyth 2019*). The aspect ratio is defined as h_{es}/λ. In this ratio, h_{es} is the billow height, measured graphically from the echosounder image. The wavelength λ is the product of the wave period, measured from the echosounder image, and the mean velocity at the height of the billows. In this subsection we explore the variability of the aspect ratio and see how it can be used to infer Ri_0.

The dimensions of observed oceanic billows are highly site-specific, with wavelength varying over two decades: *O* (1) m on estuarine lutoclines (*Held et al.*, 2019; *Tu et al.*, 2020), several meters to over 100 m in estuarine pycnoclines (*Geyer et al.*, 2017; *Tedford et al.*, 2009) and 75-700 m in the deep ocean (*Chang et al.*, 2016; *Van Haren and Gostiaux*, 2010). Atmospheric K-H billows can be even larger, with wavelengths of several km (*Fukao et al.*, 2011). In contrast to this wide variation, the aspect ratio is relatively constant. *T20* summarized 10 oceanic cases with thermohaline stratification and found that the aspect ratio ranges between 0.08 and 0.31 with mean 0.15 and standard deviation 0.08. Cases with a near-bed lutocline have yielded larger values (0.28-0.62, *Jiang and Wolanski*, 1998; 0.34-0.53, *Held et al.,* 2019); and 0.14-0.58, *T20*).

A first estimate of h_{es}/λ may be obtained by assuming that the billow height equals the thickness of the shear layer. DNS and lab experiments show that this is approximately true, though mature billows can be larger by factors of 2-3 (e.g., *Smyth and Moum, 2000*). For a K-H billow growing on an idealized shear layer, the wavelength is ~ 7 times the shear layer thickness prior to the onset of the instabilities (*Moum et al*., 2011; *Smyth and Carpenter*, 2019), suggesting an aspect ratio of 1/7=0.14. The average value 0.15 found by *T20* for the oceanic cases is close to this, but the lutocline aspect ratios are significantly larger.

Echosounder images (e.g., Figure 3) permit straightforward graphical measurement of the height and the period of a train of billows. The wavelength of the billows is approximated by multiplying the period with an estimate of the velocity at the height of maximum shear (*Smyth and Carpenter,* 2019; *Tu et al.,* 2020). The billows observed here have periods of 5-8 s. A large range of horizontal propagation velocities leads to wavelength estimates varying between 0.7-3.6 m. Aspect ratios estimated from the 6 cases described in Figure 3 vary between 0.2 and 0.71, with mean value of 0.4 and standard deviation of 0.2. Thus, both previous and present observations agree that the billow aspect ratio on near-bed lutoclines is elevated compared to that of the oceanic thermohaline cases.

A possible explanation for the increased aspect ratio of the lutocline billows is reduced Ri_0 associated with flow over the boundary. Compiling published results from previous laboratory (*Thorpe*, 1973) and DNS studies (*Fritts et al*., 2011), as well as the present DNS (see details in section 5 and Appendix B), we obtain an empirical approximation

$$Ri_0=0.25-0.39\, h_{es}/\lambda, \quad (1)$$

as shown in Figure 4.

Based on (1), the range of oceanic values compiled by *T20*, h_{es}/λ=0.15±0.08, suggests that those billows correspond to lab or DNS models with Ri_0 between 0.15 and 0.20 (thick shading on Figure 4). In the lutocline case, the well-developed K-H billows with clear braid-core structures have h_{es}/λ= 0.58, 0.41, 0.69, 0.24 and 0.54 (Figure 3a$_4$ in *Tu et al.,* 2020, Figures 3a, 3c, 3e and 3f in this study). These values are uncertain by ~50% due to our limited knowledge of the mean flow velocity, but they illustrate the use of (1), suggesting Ri_0 = 0.02, 0.09, 0, 0.15 and 0.04, respectively. These Ri_0 values are well below the Miles-Howard threshold for inviscid shear instability (Ri_0=1/4; Miles 1961; Howard 1961) and are consistent with the proximity of the benthic boundary, where shear is produced directly via bed friction and the fluid is typically well mixed. In a Monin-Obukhov boundary layer, for example, *Ri* drops linearly to zero at the boundary (e.g., *Grachev et al.,* 2015; *Scotti and White,* 2016).

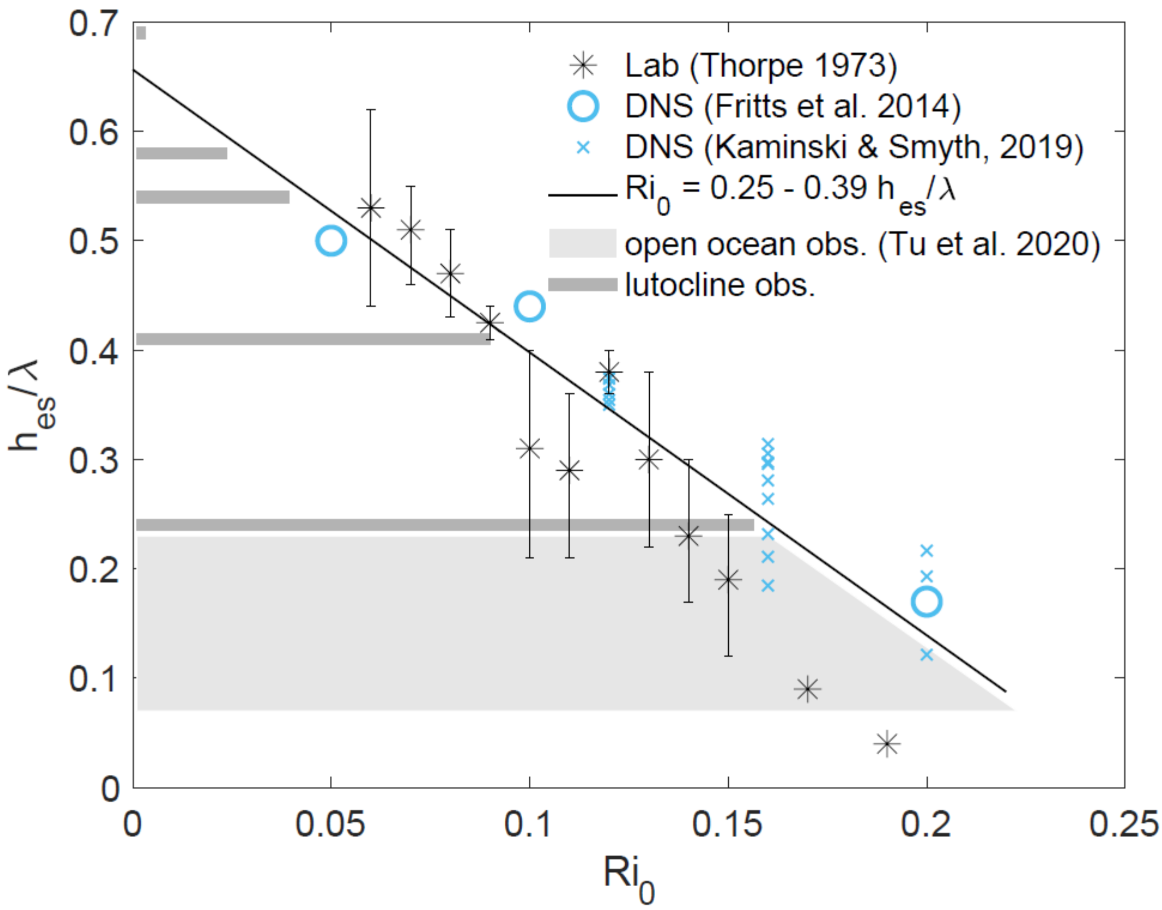

Fig. 4. Aspect ratio versus initial minimum Richardson number Ri_0. Symbols represent results from lab experiments and DNS as indicated in the legend. The straight line shows the least-squares fit (1). Shaded bars indicate *in situ* observations of aspect ratio, from which we infer Ri_0 using (1).

Jiang and Mehta (2002) made a similar comparison based on a "global Richardson number", measured directly in flows where waves already existed (whereas our parameter Ri_0 is the initial value and is measurable only in lab and DNS experiments). Jiang and Mehta found that the wave height decreases with increasing global Ri while the wavelength increases, i.e. the aspect ratio decreases. Insofar as these two variants of the Richardson number are related, the present results support those of Jiang and Mehta. Our objective here is to use the aspect ratio is to infer Ri_0, a parameter that is otherwise unmeasurable in flows where billows are already present.

5. Turbulent mixing

a. Effects of shear and stratification

To investigate the turbulent mixing associated with shear instabilities, we focus on Hour 11.5, when well-defined billows are identified and profiles of density and high frequency velocity cover the billows' vertical extent (Figure 3a). Figure 5b shows the time dependence of the echogram from which the wave-like billows' heights were approximated (Figure 5a). Although this evolution represents an unknown combination of temporal and spatial variability, it is broadly consistent with the growth, breaking and decay of a long train of K-H billows advected past an observer (e.g., *Smyth et al*., 2001; *Mashayek et al.*, 2017). From 0 to 25s, the acoustic signal is enhanced and wavelike features appear. From 25 to 50s the billows grow. From 50 to 100s clear braid-core structures are identified (also in Figure 5c), indicative of classic K-H instability; after 100s the billows appears to break down into small scale turbulence.

The squared shear, averaged vertically over ~ 0.7-1 mab, appears to correspond to the apparent billows' variability, especially an increase at ~100 s as wavelike motions become K-H billows (Figure 5d, black curve). Because the density profiles were obtained only every 0.5hr, we are obliged to assume a constant N^2 (i.e., the observed vertically averaged value) during the 150s-long period described here. The resulting *Ri* values fluctuated around 0.25 at 0-50s, identified as a pre-billow period, and drop below 0.25 after 50s when fully developed billows emerged, suggesting enhanced turbulent mixing (Figure 5e). The time-averaged S^2 appears to decrease towards the bed, whereas the N^2 increases toward bed (Figure 5f), resulting in *Ri* close to 0.25 at the mid-elevation (~ 0.8 mab, Figure 5g) which is approximately the central elevation of the observed billows.

In a standard (e.g. Monin-Obukhuv) bottom boundary layer, the shear is expected to reach its maximum at the bed. However, in our case the shear decreases towards bed. This, as observed in other FM environments (e.g., *Jaramillo et al*., 2009), is likely because the velocity inside the FM layer decays abruptly and remains low, hence the vertical gradient of current velocity is low within that layer.

b. Energy dissipation and the turbulent mass flux

The ADP measurements, analyzed using the structure function method (Appendix A), allow us to estimate values of the turbulent kinetic energy dissipation rate ε in the bottom meter of the water column in 256-second averages. This interval encompasses the passage of a train of a train of about 20 billows, together with calmer periods before and after (figure

5b). The dissipation rate varies between 7×10^{-6} and 2.5×10^{-5} $m^2\,s^{-3}$(Figure 5g, appendix A) and is balanced mainly by shear production (Appendix A, figure A1c, A1d).

It is useful to examine some diagnostics that originated in the analysis of unsheared stratified turbulence. The Ozmidov scale $L_O = \left(\frac{\varepsilon}{N^3}\right)^{1/2}$ is an estimate of the largest scale at which eddies can remain isotropic against the flattening effect of buoyancy. The buoyancy Reynolds number $Re_b = \frac{\varepsilon}{(\nu N^2)}$, where ν is the kinematic viscosity, is the four-thirds power of the ratio of L_O to the Kolmogorov scale, and thus measures the extent of the inertial subrange. Re_b must exceed 20-30 for turbulence to be maintained (*Stillinger et al.*, 1983), which is the case for the present observations ($30 < Re_b < 150$, Figure 5h).

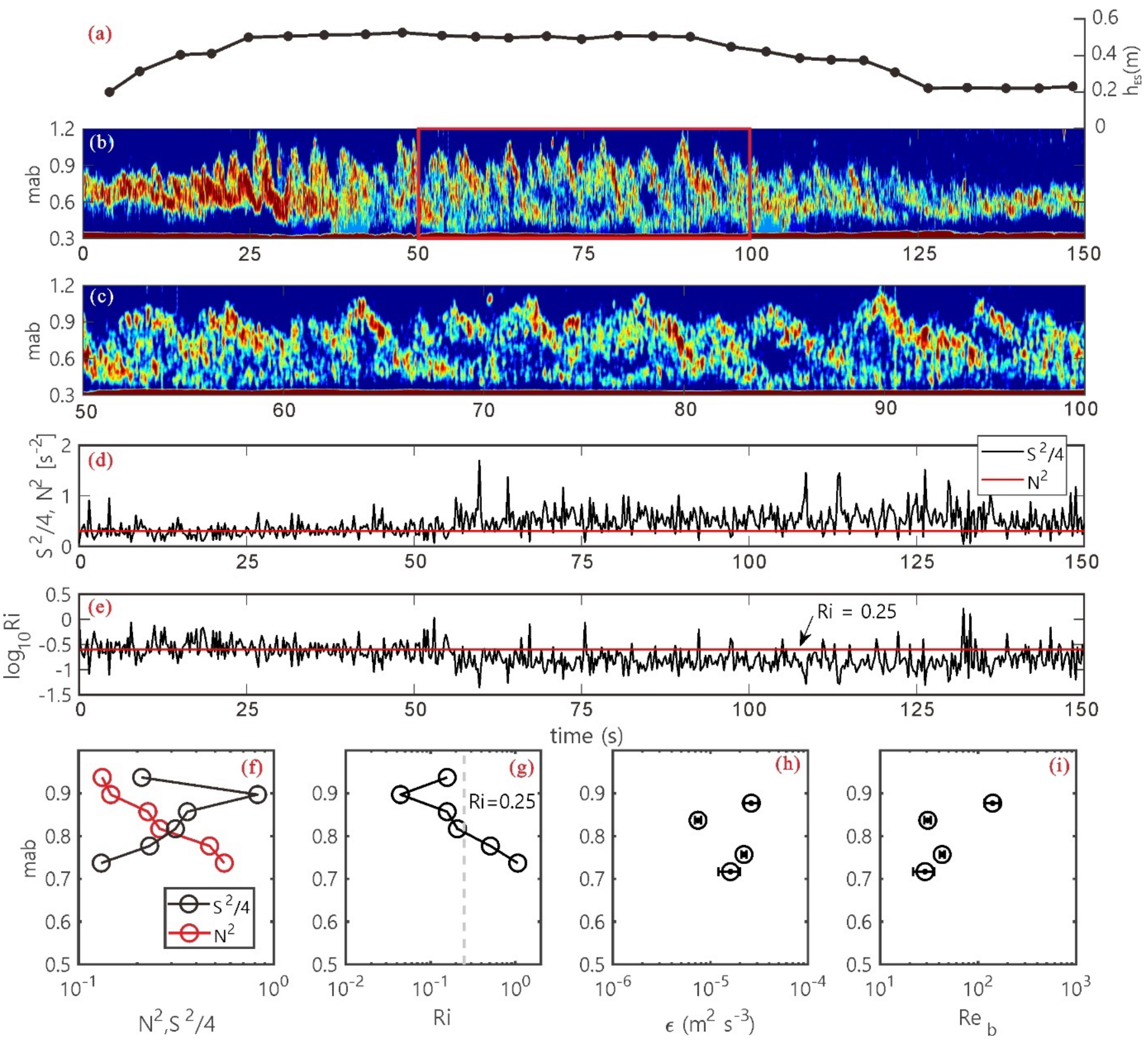

Fig. 5. Echosounder images and profiles of water-sediment mixture density and streamwise velocity for 150s near hour 11.5 (Figure 3a). (a) Billow heights as approximated by taking the vertical extent of each billow as identified from the echosounder image in (b). (c) A close-up of (b) showing the well-

defined braid-core structures as signatures of K-H billows during 50-100s. (d) time series of high-frequency, vertically averaged shear squared based on ADP velocity profiles and an assumed constant buoyancy frequency squared based on the density profiling data with the resulting *Ri* shown in (e). Vertical variations in shear and N^2, *Ri*, ε, and Re_b are shown in (f), (g), (h), and (i), respectively. These are time-averages over a 256s burst of the ADP.

The turbulent vertical buoyancy flux can be estimated as $\Gamma\varepsilon$, where Γ is the flux coefficient (e.g., *Moum*, 1996b). The flux coefficient can be approximated by the constant value 0.2 in the intermediate mixing regime with $7 < Re_b < 100$ (*Osborn*, 1980; *Shih et al.*, 2005; *Smyth*, 2020), which pertains to this study. Thus, the turbulent mass flux is $J_\rho = \Gamma\varepsilon\frac{\rho}{g}$. Inserting $\Gamma = 0.2$, $\varepsilon = 2\times10^{-5}$ m^2 s^{-3}, $\rho \approx 1015$ kg m^{-3} and $g = 9.8$ m s^{-2}, we obtain a mass flux per unit area $J_\rho = 4\times10^{-4}$ kg s^{-1} m^{-2}. If this flux acts at the height of 1 mab, the resulting mass loss in the bottom meter is 4×10^{-4} kg s^{-1} m^{-3}. As can be seen from Figure 3a$_2$, a typical SSC in the bottom meter is 15 kg m^{-3}. With our estimated mass flux, this would take ~10.4 h to erase completely. This is close to the semi-diurnal tidal period, i.e., the duration of the flood and the ebb phase. As the instabilities have been identified during both flood and ebb phases, they are expected to play a significant role in sediment transport/exchange.

c. Estimating the dissipation rate from echosounder imagery

While echosounder imagery can provide a convenient and comprehensive view of a billow train, extracting quantitative information can be challenging. *Lavery et al*. (2010) use measurements of high-frequency broadband (160-590 kHz) acoustic backscattering spectra to estimate the dissipation rate associated with K-H instabilities by fitting the observed spectra to established models. Here we explore an alternative approach that allows us to estimate the turbulent kinetic energy dissipation rate ε based on an echosounder image.

We assume that, when billows are clearly visible in an echosounder image (e.g. Figure 3c), their height is related to L_O. We therefore approximate the ratio $\frac{h_{es}}{L_O}$ by a constant *C,* and rearrange the definition of the Ozmidov scale, $L_O = \left(\frac{\varepsilon}{N^3}\right)^{\frac{1}{2}}$, to give

$$\varepsilon = C^{-2}h_{es}^2N^3. \qquad (2)$$

But is the assumption $h_{es}/L_O = constant$ valid? And if so what is its value? We address these questions using both observational and numerical data. In the Connecticut River estuary, *Geyer et al.* (2010) observed K-H billows with h_{es} = 2 m, $\varepsilon = 2.4\times10^{-4}$ m^{2}s^{-3}, and N = 0.19 s^{-1}, yielding L_O = 0.19 m and therefore h_{es}/L_O = 11. (The estimate of L_O is sensitive to the calculation method. Here we averaged values of ε, and of N, from nine locations in a billow train as given in *Geyer et al.* (2010) 's table 1, then combined the averages to get L_O. If the values are combined first, then the resulting L_O averaged, the result is 50% higher.) In the same estuary, *Holleman et al.* (2016) found h_{es}/L_O = 3m / 0.24m = 12.5. In the Kuroshio, *Chang et al.* (2016) observed large scale K-H instabilities with h_{es} ~ 100 m. Combining estimates of $N^2 = 10^{-4}$ s^{-2} and $\varepsilon = 5\times10^{-5}$ m^{2}s^{-3}, we obtain L_O = 7m and h_{es}/L_O = 14. Averaging these three estimates gives $C=h_{es}/L_O \approx 12.5$, or $C^{-2} \approx 0.0064$ in (2).

We now explore the relationship between billow height and Ozmidov scale further using a suite of 18 DNS experiments, each covering the growth, breaking and decay of a K-H billow train. These experiments are described in Appendix B, and in more detail in *Kaminski and Smyth* (2019). Figure 6 shows the growth and breakdown of the billows as observed by a "virtual echosounder" (Appendix B), as well as the temporal variations in L_O and h_{es}. The billow height h_{es} increases initially then levels off at a time that is close to t_{2d} (the time at which the kinetic energy in two-dimensional motions is a maximum, or roughly the time of maximum amplitude for the primary K-H billow; see Appendix B). Beyond this stage, h_{es} increases but only slightly. On the other hand, L_O is small during the initial growth of h_{es} but then increases rapidly to a maximum near the time t_{3d} (when 3d motions are most energetic), then decreases rapidly back to zero. Because that maximum is the only non-arbitrary value of L_O that can be defined for a K-H event, our goal in this DNS analysis is to predict its value, and ultimately that of the corresponding ε. In the observational analyses discussed above, L_O is a typical value for the region containing the instability, defined subjectively. The distinction between this and the maximum value of L_O is secondary and cannot be made with the available data. In the example shown in Figure 6, h_{es} and $10L_O$ are nearly equal for $t\sim t_{3d}$, suggesting $h_{es}/L_O \sim 10$, very similar to the observational estimates.

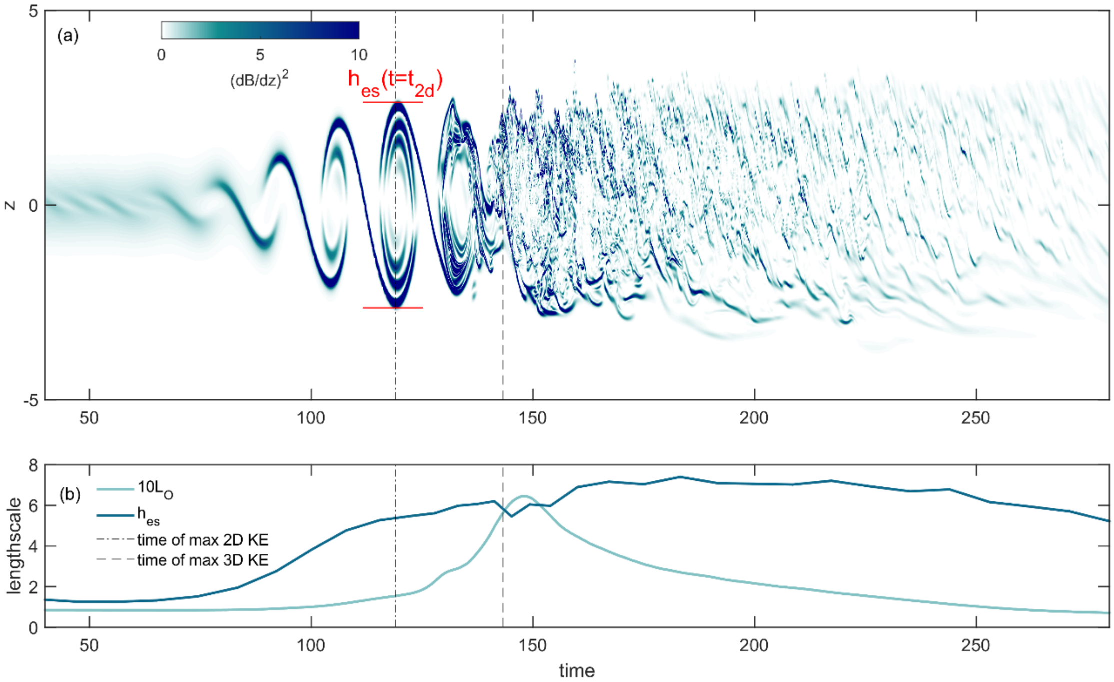

Fig. 6. Results from example DNS with Re=2000, Ri_0=0.12, Pr=1 (from *Kaminski and Smyth,* 2019). Details of the DNS are given in Appendix B. (a) Proxy echosounder image extracted from DNS. The nondimensional squared vertical density gradient is plotted. (b) Nondimensional length scales 10 L_O and h_{es} versus nondimensional time. Vertical lines show t_{2d} and t_{3d}, the times of maximum kinetic energy in 2d and 3d motions (*Smyth et al.,* 2005).

The ratio h_{es}/L_O in a DNS also depends on other parameters of the initial state: the initial Richardson and Reynolds numbers and the amplitude of the initial noise field. Combining results for various values of these parameters (Figure 7) we find that the ratio is generally ~*O* (10) but can vary significantly. We conclude that (2), with $C=12.5$ as suggested previously (or $C^{-2}=0.0064$) gives a useful first estimate of the *maximum* dissipation rate attained by a breaking K-H billow.

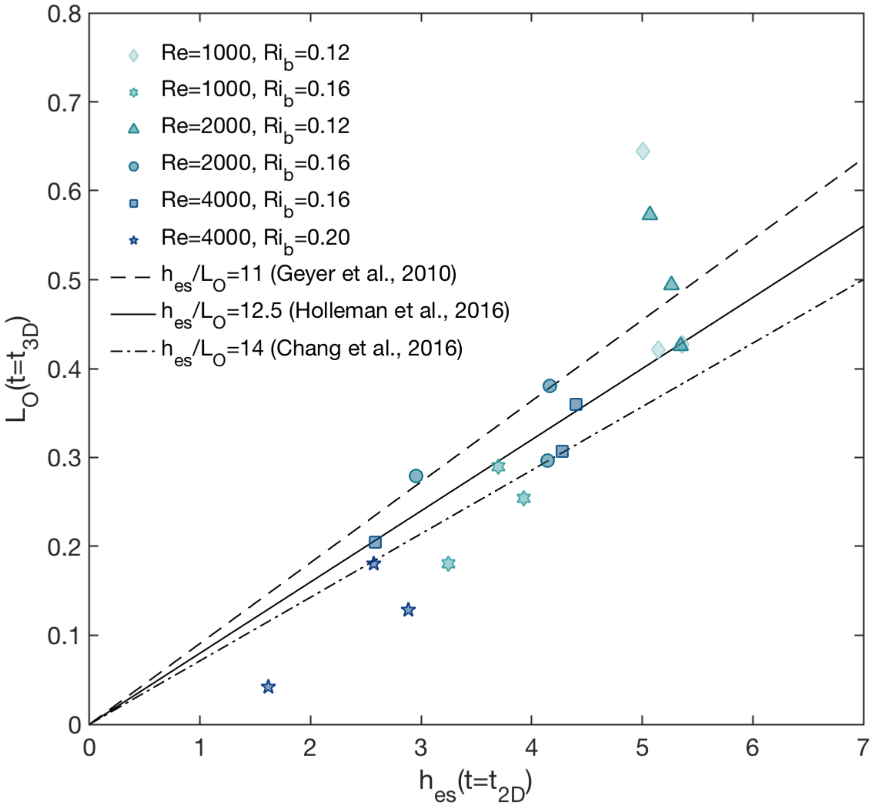

Fig. 7. Ozmidov scale L_O at t_{3d} versus billow height h_{es} at $t=t_{2d}$, from 18 DNS runs as described by *Kaminski and Smyth* (2019). An example is shown in figure 6. *Re* and *Ri* are as given in the legend. Each symbol type represents three simulations with initial turbulence amplitude A=0.0025, 0.01 and 0.05.

6. Discussion

The present observations lie in an extreme parameter regime and therefore offer an interesting test of (2). Unfortunately, only one of the examples shown in figure 3 has billows located in the lowermost meter of the flow, where ADP measurements are available (figure 3a). Moreover, the structure function estimate of ε is available only as an average over the 256-second ADP burst, in which billows are present only part of the time. The Ozmidov scale, based on segment-averaged value of ε, and N, is L_O = 0.01m, an order of magnitude smaller even than the other estuarine cases (*Geyer et al*., 2010; *Holleman et al*., 2016). The disturbance height ranges between 0.5m (when billows are present) and 0.2m (when they are not). Using the value measured when billows are clearly present, we find h_{es}/L_O ~50. Phrased differently, the structure function estimate of ε is smaller by an order of magnitude than the value predicted by the scaling (2) with C=12.5.

In summary, previous observations supported by the present DNS give consistent values of h_{es}/L_O near 12.5. This suggests that (2), with C=12.5, is a useful approximation for ε. In contrast, our lutocline observation at hour 11.5 gives a much larger value $h_{es}/L_O \sim 50$. This distinction may be interpreted in three ways:

1. *Uncertainty in the structure function estimate of ε:* The structure function method (Appendix A) may underestimate ε. The method is based on Kolmogorov's theory of the inertial subrange, and thus neglects the potentially important effects of stratification and boundary proximity. The required measurements of the fluctuating velocity are missing from some parts of the water column. But the deficit in ε needed to account for the discrepancy in h_{es}/L_O is an order of magnitude, whereas the turbulent kinetic energy balance used to test the method suggests at most a factor-of-two deficit (Appendix A).
2. *Time dependence of billow length scales:* Our hour 11.5 observation may represent a time interval not characteristic of turbulent billows. As shown by the DNS (Figure 6), young billows are tall and clearly visible in echosounder images, precisely because they are not yet fully turbulent (*Smyth et al., 2001*). Graphical estimates of h_{es} are often made at this stage. In contrast, our estimate of ε for the lutocline case is an average over a 256-second period that includes young billows, mature billows in which ε is larger, and quiescent periods in which ε is again small.
3. *Differences in near-lutocline flows:* There may be a genuine physical difference in the lutocline case. This possibility is consistent with the tendency of the aspect ratio h_{es}/λ to be relatively large in lutocline cases (section 4.2), which appears to be real. As one explanation, one may think of h_{es} as a measure of the potential energy stored in a young billow. More specifically, the potential energy is $\sim h_{es}^2N^2$ (*Dillon and Park*, 1987). When the billow breaks, that potential energy is converted to turbulent kinetic energy and, ultimately, to internal energy via ε. So in the lutocline case, ε is smaller than would be expected given the amount of potential energy available. It could be that the lutocline billows lose energy to some other mechanism besides viscous dissipation, such as radiation of gravity waves into the surrounding sediment-stratified fluid.

7. Summary and future work

After a shipboard observational campaign in a hyperturbid estuarine tidal channel, we analyzed echosounder images, vertical profiles of velocity and suspended sediment-dominated density, as well as the dissipation rate of turbulent kinetic energy ε as derived using the structure function method. The main findings are summarized as follows,

- Waves, instability, and turbulence are seen within FM layers at both flood and ebb tide.
- Echosounder images, together with mean velocity profiles, allow estimation of the aspect ratio and therefore of the initial Richardson number characterizing the flow prior to instability growth.
- The aspect ratio is larger for billows on estuarine lutoclines than those observed in oceanic interior. This may be related to the smaller initial minimum Richardson number.
- The turbulent mass flux can be significant in suspending sediment over a tidal cycle.
- Echosounder images, together with density profiles, allow estimates of the turbulent dissipation rate ε. While valid for a broad range of oceanic conditions, this estimate appears to be too small when applied to the lutocline observations. The difference may reflect insufficient measurements or it may indicate a physical difference in lutocline billows.

These results, including details of the interactions between velocity shear and mud-induced stratification, periodic occurrence and collapse of shear instability, and turbulent mixing, have broadened our understanding of fluid dynamics in a hyperturbid boundary layer. Our results may also suggest realistic modeling scenarios and allow for better predictions of sediment entrainment, mixing, and dispersion of FM in hyperturbid estuarine channels.

Three caveats suggest lines of future investigation.

- Though rare, our observations include regions where SSC values approach 100g/L, suggesting the possibility of variable viscosity (Appendix C).
- In interpreting the observations in terms of shear instability and the gradient Richardson number, we implicitly assume that these sediment-stratified flows respect the Boussinesq approximation. In our observations, that density typically changes by no more than 8% over the lowest meter of the water column (Fig. 3). While this change is small compared with previous cases where the Boussinesq approximation

has been assumed (e.g., *Daly and Pracht*, 1968; *Schatzmann and Policastro*, 1984), and in particular where the Boussinesq value 1/4 for the critical Richardson number has been applied (*Trowbridge and Kineke*, 1994), it is possible that this and other parameter values are affected by non-Boussinesq effects. Future research should address this question.

- While the parameterization (2) is useful, we must understand its boundaries of validity, beginning with why it requires adjustment in the lutocline case. This will require more extensive DNS explorations as well as more targeted observations. The present turbulent mixing estimates are time-averaged over a few minutes thus are not able to resolve the details of individual billows (period ~ 5 - 8 seconds). Future work should focus on resolving the fine temporal and spatial scales of motion within the braid and core areas, and velocity measurements should cover the water column more completely.

Acknowledgments.

The contribution of J. Tu was with the support of the National Natural Science Foundation of China (NSFC-41906052). J. Tu, F. Sun, and D. Fan were supported by NSFC-41776052 and the Innovation Program of Shanghai Municipal Education Commission (2021-01-07-00-07- E00093). A. Kaminski was supported by the U.S. National Science Foundation under grant OCE-1537173 and OCE-1657676. W. Smyth was supported by the U.S. National Science Foundation under grant OCE-1830071. We acknowledge high-performance computing support on Cheyenne (doi:10.5065/D6RX99HX) provided by NCAR's Computational and Information Systems Laboratory, sponsored by the U.S. National Science Foundation.

Data Availability Statement.

The observational and DNS simulations data used in this study are publicly available at https://zenodo.org/record/5558794#.YWGusBpByUk.

APPENDIX A

TKE dissipation rate estimates using structure function

Following *Wiles et al.* (2006), the TKE dissipation rate ε_i was estimated along beam *i* using the second order structure function,

$$D(z,r) = [b'(z) - b'(z-r)]^2 \qquad \text{(A1)}$$

Where *b'(z)* is the along beam velocity fluctuation at a height *z* above the bed, *r* is the along-beam distance between velocity measurements and the overbar denotes a segment time average (256s).

According to the Kolmogorov's inertial subrange theory, the structure function can be expressed as

$$D(z,r) = C_v^2 \varepsilon^{2/3} r^{2/3} \qquad \text{(A2)}$$

Where $C_v^2 = 2.1$ is an empirical constant (*Pope*, 2000). To obtain estimates of ε, the second-order structure function $D(z,r)$ is fitted to a linear equation using MATLAB's robust fit algorithm,

$$D(z,r) = Ar^{2/3} + n \qquad \text{(A3)}$$

The slope of the regression, *A*, is related to the dissipation by

$$A = C_v^2 \varepsilon^{2/3} \qquad \text{(A4)}$$

and *n* is an offset related to the Aquadopp noise variance, which is assumed to be independent of *r*. TKE dissipation rates were estimated from the 256s segment detrended velocity records (data points =1024) using equations A2-A4. The separation distance *r* was limited to the distance to the boundary (*Mullarney and Henderson*, 2012). Following *Thomson* (2012), *n* is obtained as a free parameter in the fit and further used for quality control by accepting only $n < 2\sigma_{u'}^2$ and $n \ll A\, r^{2/3}$, where $\sigma_{u'} = 0.0175$ m/s is a nominal velocity uncertainty (see Text2 in the supplemental material). The goodness of the fit is assessed by adjusted *R* squared $R_{adj}^2 = 1 - \frac{(1-R^2)(m-1)}{m-k-1}$ and normalized standard error by the mean value (NSE = SE/MEAN). Here R^2 is the ordinary square of correlation coefficient between observed and fitted structure functions, *m* is the total sample size, $k = 1$ is the number of variables. Only estimates with $R_{adj}^2 > 0.7$ and NSE < 0.3 were retained for further analysis. Though somewhat subjective, visual comparison of the observed and fitted data indicates that the threshold values defined above assure good data quality. Dissipation estimates from three beams were log-averaged to provide a single dissipation estimate for each elevation for a given segment. An example of the estimation of dissipation using structure function is shown in Figure A1a and A1b. As the available velocity records of ADP were limited by signal attenuation by the FM. Therefore, available dissipation estimates were even less given that at least three velocity points were required to obtain a dissipation estimate, and some of the obtained dissipation rates were further excluded if they failed to pass the quality control described earlier.

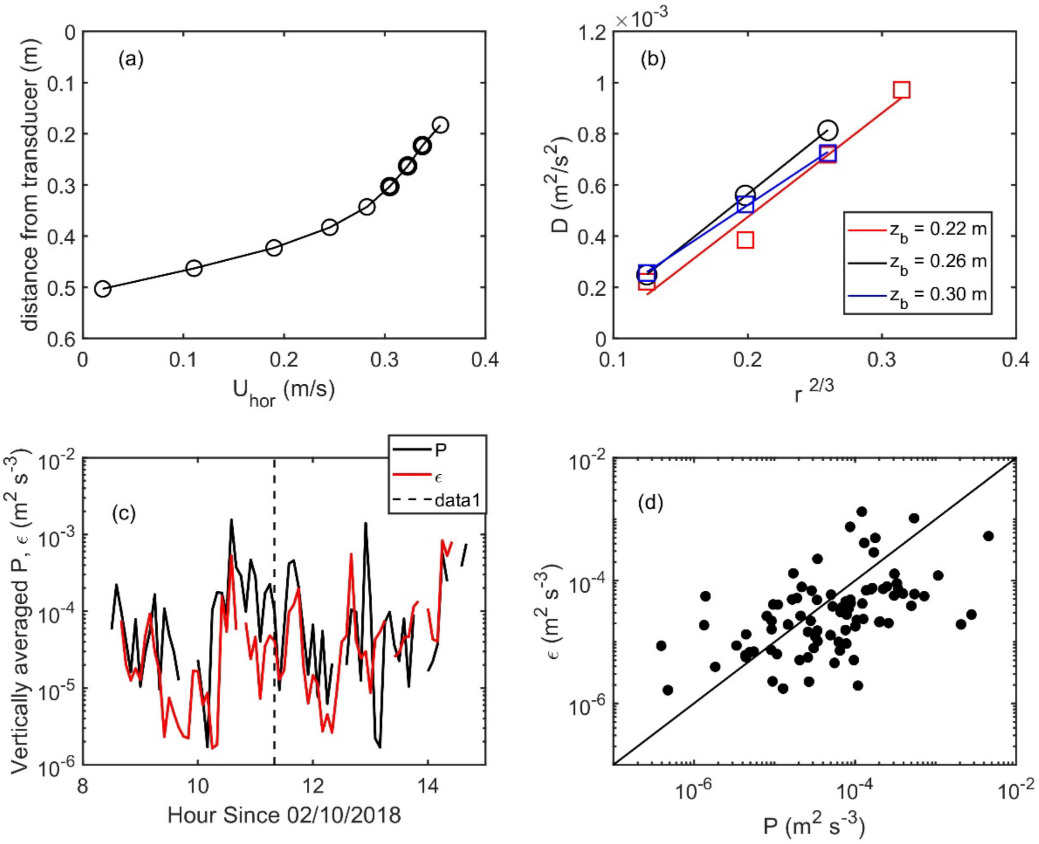

Fig. A1. (a) Velocity measurements of Aquadopp HR on 2 October 11:20 local time (segment 35, indicated by dashed line in (c)). (b) Structure function and associated fits (lines) to Eq.4 for a single beam from Aquadopp HR at the same segment as (a). z_b represents distance below the Aquadopp HR transducer (m). Comparisons between the estimated dissipation and production are also shown in (c) and (d).

The shear production ($P = -\langle u'w' \rangle \frac{\partial u}{\partial z}$) was calculated as an independent parameter for comparison. The estimate of current shear $\frac{\partial u}{\partial z}$ is straightforward using the segment averaged streamwise velocities at different elevations. However, the calculation of Reynolds stress

$\langle u'w' \rangle$ can be complicated by nonturbulent motions, counter-gradient flux, and noise floor (*Scully et al.*, 2011; *Walter et al.*, 2011). To address these issues, we fit the observed cospectra to the model proposed by *Kaimal et al.* (1972):

$$\frac{kS_{uw}(k)}{\langle u'w' \rangle} = \frac{0.88(\frac{k}{k_0})}{1 + 1.5(\frac{k}{k_0})^{\frac{5}{3}}} \tag{A5}$$

where S_{uw} is the cospectra of each ADP segment estimated using the Welch method (*Welch*, 1967) with 50% overlap and applying a Hamming window. The frequency f is then converted to wavenumber k via $k = 2\pi f/U$, making Taylor's frozen turbulence assumption. A two-parameter least-square fitting can be used with the observed $S_{uw}(k)$, to obtain estimates of Reynolds stress $\langle u'w' \rangle$ and the runoff wavenumber k_0. We refer the reader to *Tu et al.* (2019) for a detailed description of the Kaimal fitting method. As can be seen from Figure A1c and A1d, the dissipation rate derived from structure function and the shear production obtained from independent Kaimal fit method roughly agree with each other, suggesting that the structure function method provides reliable dissipation estimates.

Figure A1d shows that the shear production is somewhat larger than dissipation rate with a mean value of P/ε being 1.7. Given that the fluid flow is strongly stratified by the suspended sediment, it is likely that the imbalance between P and ε is attributable to buoyancy destruction by sediment. Assuming stationary, homogeneous turbulence, the energy balance is given by $P = B + \varepsilon$. *Jones and Monismith* (2008) found that $P/\varepsilon = 3.3$ and argued that the sediment concentration gradient near bed might account for the disparity between P and ε. If the sediment settling flux and the vertical turbulent flux of sediment are balanced (consistent with the assumption of stationarity), the turbulent buoyancy flux B can be written as minus the settling flux (*Green and McCave* 1995),

$$B = \frac{g(\rho_s - \rho_w)}{\rho_s \rho_w} SSC \cdot w_s \tag{A6}$$

where g is gravity acceleration, ρ_s is sediment density, ρ_w is the fluid density, and w_s is the sediment settling velocity. Using a $w_s = 4.6\times10^{-4}$ m s^{-1}, ρ_s=1320 kg m^{-3} for the flocculated sediment in Changjiang estuary (*Tang*, 2007), and SSC = 20 kg m^{-3} (Figure 2a$_1$) we obtain an estimate of B~ 2×10^{-5} m^2 s^{-3}. This value is at the same magnitude as P (4.9×10^{-5} m^2 s^{-3}) and ε (2.8×10^{-5} m^2 s^{-3}). Although just an estimate of order of magnitude, the buoyancy flux by mixing of suspended sediment explains the discrepancy between shear production and dissipation. This suggests that the structure function estimate of ε is reliable for the present observations.

APPENDIX B

DNS methods

The direct numerical simulations are based on the Boussinesq approximation to the Navier-Stokes equations. The computation domain is rectilinear. Boundary conditions are periodic in both horizontal directions, free-slip, permeable and constant-buoyancy at the top and bottom. The streamwise periodicity length matches the wavelength of the fastest-growing shear instability.

The initial state is a stratified shear layer with mean streamwise velocity and buoyancy defined by

$$\frac{U}{\Delta U} = \frac{B}{\Delta B} = \tanh\frac{z}{h} \qquad \text{(A8)}$$

For the example shown in figure 6, the constants $\Delta U, \Delta B$ and h are chosen such that the initial Reynolds number $Re = h\Delta U/\nu = 2000$, the Prandtl number $Pr = \nu/\kappa = 1$ and the initial Richardson number $Ri = h\frac{\Delta B}{\Delta U^2} = 0.12$. To this initial state is added a small-amplitude, quasi-random noise field to trigger the instability. Further details may be found in *Kaminski and Smyth* (2019), where the simulation shown in figure 6 is entry #10 in table 1.

Echosounder response is approximated by the squared buoyancy gradient $\left(\frac{\partial b}{\partial z}\right)^2$. To approximate the response of a fixed echosounder to instabilities advecting downstream at speed ΔU, we compute a profile of the squared buoyancy gradient at a point that moves upstream at a constant speed ΔU, viz: $\left(\frac{\partial b}{\partial z}\right)^2]_{x=-\Delta U t}$. If the observation point $x = -\Delta U t$ encounters a boundary, it is moved a distance L_x to the right in accordance with the periodic boundary condition.

At any given time, the billow height h_{es} is computed as the vertical distance between the upper and lower maxima in the buoyancy gradient $\left(\frac{\partial b}{\partial z}\right)^2$. The dissipation rate ε is calculated from the strain rate tensor at each point in space and averaged both horizontally and over the vertical extent of the turbulent shear layer. The corresponding squared buoyancy frequency N^2 is calculated from the mean buoyancy profile and similarly averaged over the shear layer. The latter two quantities are combined to obtain the Ozmidov scale.

Another useful diagnostic is the specific kinetic energies (one half the squared velocity) contained in various components of the motion (*Smyth et al., 2005*). The mean kinetic energy is the volume average of $U^2/2$, where $U(z,t)$ is the streamwise velocity averaged over the horizontal directions x and y. Subtracting U from the total velocity field and averaging over y gives $\vec{u}_{2d}(x, z, t)$, the 2d component of the motion that is dominated by the K-H billow. Subtracting U and $\vec{u}_{2d}$, from the total velocity field isolates the 3d motions associated with secondary instabilities and turbulence. At the beginning of an instability event, the mean flow is dominant. The 2d component associated with the primary K-H billows grows exponentially then saturates, reaching its maximum amplitude at time t_{2d}. As secondary instabilities sap the energy of the billows, the 3d component of the motion grows, and its kinetic energy reaches a maximum at the later time t_{3d}. In the end, the disturbances dissipate and the energy is again contained in the mean flow.

APPENDIX C

The impact of SSC on viscosity

Although numerous empirical formulas express the relationship between SSC and viscosity, there is no consensus on a general expression (*Mehta*, 2013). *Thomas* (1963) proposed a formula for viscosity that can be applied to SSC exceeding several hundreds of g/L with particles in the size range between 0.1 and 20 µm (close to mean grain size of 8µm in this study),

$\eta = \eta_w \left(1 + 2.5\Phi_{vf} + 10.05\Phi_{vf}^2 + 0.062\exp\left(\frac{1.875\Phi_{vf}}{1-1.595\Phi_{vf}}\right)\right)$, where η_w is the dynamic viscosity of water, $\Phi_{vf} = \frac{SSC(\rho_s-\rho_w)}{\rho_s(\rho_f-\rho_w)}$ is the floc volume fraction (*Mehta*, 2013). Here, ρ_s=2650 g/L is the sediment particle density, ρ_w is the water density, and ρ_f is the floc density. In the same estuary, *Guo et al*. (2017) found ρ_f ~ 1300 g/L.

As can be seen in Figure 3, the SSC at the billows elevation generally varies between 10-100 g/L, this gives a viscosity between $1.1\eta_w$ and $2\eta_w$. *Wang* (2021) conducted rheological experiments using mud from the same estuary and found $\frac{\eta}{\eta_w} \sim 1.3$ at SSC ~ 100 g/L. Similarly, *Fei* (1982) compiled experimental results using fine sediment with similar size (d50 = 6-9 μm) as present study. They found $\frac{\eta}{\eta_w}$ values varying between 1.02-1.65 given SSC of 10-100 g/L. Regarding the DNS, *Harang et al.* (2014) show that, at large Reynolds number (Re > ~1000), the mud viscosity has no influence on the development of the primary instability, which is used to derived key parameters (e.g., wave height) for the inference of turbulence. The relevant Reynolds number is $Re = u\delta/\nu$, where u, δ and ν are half-velocity difference across the layer, half-thickness of the shear layer, and fluid kinematic viscosity. Given typical values of u~ 0.25 m/s, δ ~0.5 m (See the six cases in Figure 3), and $\nu < 2\nu_w = 2\times10^{-6}$ estimated above (where ν_w is the kinematic viscosity of clear water), we arrive at $Re > 6\times10^4$, indicating turbulent flow.

From an observational perspective, researchers may use SSC and velocity profiles to infer the depth-dependent viscosity on basis of momentum equation (e.g., *Vinzon and Mehta*, 2000; *Traykovski et al.*, 2015). The viscosity derived using this method, however, is termed as a total viscosity including turbulent eddy viscosity (ν_t) and fluid-mud viscosity (ν_m); Thus, in turbulent flows, ν_t dominates while in laminar flows ν_m dominates (*Traykovski et al.*, 2015). The Reynolds number $Re > 6\times10^4$ estimated above indicates that the periods with shear instabilities and internal waves are generally turbulent, hence eddy viscosity plays a key role. Therefore, it is likely that the suspended sediment has minor impact on the total viscosity, and thus on flow dynamics, except very few periods with extremely high SSC approaching 100g/L.

REFERENCES

Becker, M., C. Maushake, and C. Winter (2018), Observations of Mud-Induced Periodic Stratification in a Hyperturbid Estuary, *Geophys. Res. Lett.*, *45*(11), 5461-5469, doi: 10.1029/2018GL077966.

Bruens, A., J. Winterwerp, and C. Kranenburg (2012), Physical and numerical modeling of the entrainment by a high-concentration mud suspension, *J. Hydraul. Eng.*, *138*(6), 479-490.

Burchard, H., H. M. Schuttelaars, and D. K. Ralston (2018), Sediment Trapping in Estuaries, *Ann. Rev. Mar. Sci.*, 10(1), 371-395, doi:10.1146/annurev-marine-010816-060535.

Carpenter, J. R., G. A. Lawrence, and W. D. Smyth (2007), Evolution and mixing of asymmetric Holmboe instabilities, *J. Fluid Mech.*, *582*, 103-132, doi:10.1017/S0022112007005988.

Caulfield, C. (2021), Layering, instabilities, and mixing in turbulent stratified flows, *Ann. Rev. Fluid Mech.*, 53, 113-145.

Chang, M. H., S. Y. Jheng, and R. C. Lien (2016), Trains of large Kelvin-Helmholtz billows observed in the Kuroshio above a seamount, *Geophys. Res. Lett.*, *43*(16), 8654-8661.

Dai, Q., H. X. Shan, W. L. Cui, Y. G. Jia (2011), A laboratory study on the relationships between suspended sediment content and the conductivity and their influencing factors. *Acta Oceanol. Sin.*, 33: 88-94 (in Chinese with English abstract).

Dai, Z., S. Fagherazzi, X. Mei, J. Chen, and Y. Meng (2016), Linking the infilling of the North Branch in the Changjiang (Yangtze) estuary to anthropogenic activities from 1958 to 2013, *Mar. Geol.*, *379*, 1-12.

Dillon, T. M., and Park, M. M. (1987), The available potential energy of overturns as an indicator of mixing in the seasonal thermocline, *J. Geophys. Res.*, 92 (C5), 5345– 5353, doi:10.1029/JC092iC05p05345.

Fei, X.J. (1982) Viscosity of high concentration muddy water, *J. Hydraul. Eng.*, (03), 57-63 (in Chinese).

Fritts, D. C., G. Baumgarten, K. Wan, J. Werne, and T. Lund (2014), Quantifying Kelvin-Helmholtz instability dynamics observed in noctilucent clouds: 2. Modeling and interpretation of observations, *J. Geophys. Res. Atmos.*, 119(15), 9359-9375.

Fukao, S., H. Luce, T. Mega, and M. K. Yamamoto (2011), Extensive studies of large-amplitude Kelvin–Helmholtz billows in the lower atmosphere with VHF middle and upper atmosphere radar, *Quart. J. Roy. Meteor. Soc.,* 137(657), 1019-1041.

Geyer, W. R., A. C. Lavery, M. E. Scully, and J. H. Trowbridge (2010), Mixing by shear instability at high Reynolds number, *Geophys. Res. Lett.*, *37*(22).

Geyer, W. R., D. K. Ralston, and R. C. Holleman (2017), Hydraulics and mixing in a laterally divergent channel of a highly stratified estuary, *J. Geophys. Res. Oceans*, *122*(6), 4743-4760, doi:10.1002/2016jc012455.

Grachev, A. A., E. L. Andreas, C. W. Fairall, P. S. Guest, and P. O. G. Persson, 2015: Similarity theory based on the Dougherty-Ozmidov length scale. *Quart. J. Roy. Meteor. Soc*., 141 (690), 350 1845–1856.

Green, M. O., and I. McCave (1995), Seabed drag coefficient under tidal currents in the eastern Irish Sea, *J. Geophys. Res. Oceans*, *100*(C8), 16057-16069.

Guo, C., He, Q., Guo, L., and Winterwerp, J. C., 2017, A study of in-situ sediment flocculation in the turbidity maxima of the Yangtze Estuary, *Estuar. Coast. Shelf Sci.*, v. 191, p. 1-9.

Harang, A., Thual, O., Brancher, P., & Bonometti, T. (2014). Kelvin–Helmholtz instability in the presence of variable viscosity for mudflow resuspension in estuaries, *Environ. Fluid Mech*., 14(4), 743-769.

Hebert, D., J. Moum, C. Paulson, and D. Caldwell (1992), Turbulence and internal waves at the equator. Part II: Details of a single event, *J. Phys. Oceanogr.*, 22(11), 1346-1356.

Held, P., K. Bartholomä-Schrottke, and A. Bartholomä (2019), Indications for the transition of Kelvin-Helmholtz instabilities into propagating internal waves in a high turbid estuary and their effect on the stratification stability, *Geo-Mar. Lett.*, doi:10.1007/s00367-019-00564-4.

Held, P., K. Schrottke, and A. Bartholomä (2013), Generation and evolution of high-frequency internal waves in the Ems estuary, Germany, *J. Sea Res.*, *78*, 25-35.

Holleman, R., W. Geyer, and D. Ralston (2016), Stratified Turbulence and Mixing Efficiency in a Salt Wedge Estuary, *J. Phys. Oceanogr.*, *46*(6), 1769-1783.

Howard, L. N. (1961), Note on a paper of John W. Miles, *J. Fluid Mech.*, *10*(4), 509-512.

Jaramillo, S., A. Sheremet, M. Allison, A. Reed, and K. Holland (2009), Wave-mud interactions over the muddy Atchafalaya subaqueous clinoform, Louisiana, United States: Wave-supported sediment transport, *J. Geophys. Res. Oceans*, *114*(C4).

Jiang, J., and Mehta, A., 2002, Interfacial instabilities at the lutocline in the Jiaojiang estuary, China, Proceedings in Marine Science, Volume 5, Elsevier, p. 125-137.

Jiang, J., and Wolanski, E. (1998). Vertical mixing by internal wave breaking at the lutocline, Jiaojiang River estuary, China. *J. Coast. Res.*, 14, 1426–1431.

Jones, N. L., and S. G. Monismith (2008), The influence of whitecapping waves on the vertical structure of turbulence in a shallow estuarine embayment, *J. Phys. Oceanogr., 38*(7), 1563-1580.

Kaimal, J., J. Wyngaard, Y. Izumi, and O. Coté (1972), Spectral characteristics of surface-layer turbulence, *Quart. J. Roy. Meteor. Soc., 98*(417), 563-589.

Kaminski, A., and W. Smyth (2019), Stratified shear instability in a field of pre-existing turbulence, *J. Fluid Mech.*, *862*, 639-658.

Kineke, G., and R. Sternberg (1992), Measurements of high concentration suspended sediments using the optical backscatterance sensor, *Mar. Geol.*, *108*(3-4), 253-258.

Kineke, G., and R. Sternberg (1995), Distribution of fluid muds on the Amazon continental shelf, *Mar. Geol.*, *125*(3-4), 193-233.

Klymak, J. M., and S. M. Legg (2010), A simple mixing scheme for models that resolve breaking internal waves, *Ocean Model.*, *33*(3), 224-234, https://doi.org/10.1016/j.ocemod.2010.02.005.

Lavery, A. C., Chu, D., and Moum, J. N., 2010, Observations of Broadband Acoustic Backscattering From Nonlinear Internal Waves: Assessing the Contribution From Microstructure, *IEEE J. Ocean. Eng.*, v. 35, no. 4, p. 695-709.

Lee, X. (1997), Gravity waves in a forest: a linear analysis, *J. Atmos. Sci.* 54, 2574-2585.

Mashayek, A., C. P. Caulfield, and W. R. Peltier (2017), Role of overturns in optimal mixing in stratified mixing layers, *J. Fluid Mech.*, 826, 522-552, doi:10.1017/jfm.2017.374.

McAnally, W. H., C. Friedrichs, D. Hamilton, E. Hayter, P. Shrestha, H. Rodriguez, A. Sheremet, A. Teeter, and A. T. C. o. M. o. F. Mud (2007), Management of fluid mud in estuaries, bays, and lakes. I: Present state of understanding on character and behavior, *J. Hydraul. Eng.*, *133*(1), 9-22.

Mehta, A. J. (2013). An introduction to hydraulics of fine sediment transport (Vol. 38): World Scientific Publishing Company.

Miles, J. W. (1961), On the stability of heterogeneous shear flows, *J. Fluid Mech.*, *10*(4), 496-508.

Moum, J.N., (1996a), Energy-containing scales of turbulence in the ocean thermocline, *J. Geophys. Res.*101, 14095.

Moum, J.N., (1996b), Efficiency of mixing in the main thermocline, *J. Geophys.Res.*101, 57.

Moum, J., D. Farmer, W. Smyth, L. Armi, and S. Vagle (2003), Structure and generation of turbulence at interfaces strained by internal solitary waves propagating shoreward over the continental shelf, *J. Phys. Oceanogr.*, *33*(10), 2093-2112.

Mullarney, J. C., and S. M. Henderson (2012), Lagrangian measurements of turbulent dissipation over a shallow tidal flat from pulse coherent Acoustic Doppler Profilers, *Coast. Eng. Proc.*, 1-12.

Osborn, T. (1980), Estimates of the local rate of vertical diffusion from dissipation measurements, *J. Phys. Oceanogr.*, *10*(1), 83-89.

Pope, S. B. (2000), *Turbulent flows*, Cambridge University Press.

Salehipour, H., Caulfield, C., and Peltier, W. (2016). Turbulent mixing due to the Holmboe wave instability at high Reynolds number, *J. Fluid Mech.* https://doi.org/10.1017/jfm.2016.488.

Scarlatos, P. D., and A. J. Mehta (1993), Instability and Entrainment Mechanisms at the Stratified Fluid Mud-Water Interface, *Nearshore and estuarine cohesive sediment transport*, 205-223.

Scotti, A., and B. White, 2016: The mixing efficiency of stratified turbulent boundary layers. *J. Phys. Oceanogr.*, **46** (10), 3181–3191, doi:10.1175/JPO-D-16-0095.1.

Scully, M. E., W. R. Geyer, and J. H. Trowbridge (2011), The influence of stratification and nonlocal turbulent production on estuarine turbulence: An assessment of turbulence closure with field observations, *J. Phys. Oceanogr.*, *41*(1), 166-185.

Seim, H. E., and M. C. Gregg (1994), Detailed observations of a naturally occurring shear instability, *J. Geophys. Res. Oceans*, *99*(C5), 10049-10073.

Shih, L. H., J. R. Koseff, G. N. Ivey, and J. H. Ferziger (2005), Parameterization of turbulent fluxes and scales using homogeneous sheared stably stratified turbulence simulations, *J. Fluid Mech.*, *525*, 193-214.

Smyth, W.D., 2020: “Marginal instability and the efficiency of ocean mixing”, *J. Phys. Oceanogr.* **50** (8), 2141-2150. https://doi.org/10.1175/JPO-D-20-0083.1

Smyth, W.D., J.D Nash and J.N. Moum, 2005: “Differential diffusion in breaking Kelvin-Helmholtz billows”, *J. Phys. Oceanogr*. **35** (6), 1004-1022.

Smyth, W., J. Moum, and D. Caldwell (2001), The efficiency of mixing in turbulent patches: Inferences from direct simulations and microstructure observations, *J. Phys. Oceanogr.*, 31(8), 1969-1992.

Smyth, W., J. Moum, and J. Nash (2011), Narrowband oscillations in the upper equatorial ocean. Part II: Properties of shear instabilities, *J. Phys. Oceanogr.*, *41*(3), 412-428.

Smyth, W.D. and J.R. Carpenter, 2019, *“Instability in Geophysical Flows”,* Cambridge University Press.

Smyth, W.D., J.R. Carpenter and G.A. Lawrence (2007): “Mixing in symmetric Holmboe waves”, *J. Phys. Oceanogr.* **37** (6) 1566-1583.

Smyth, W., J. Nash, and J. Moum (2019), Self-organized criticality in geophysical turbulence, *Sci. Rep.*, *9*(1), 3747.

Smyth, W. D., and J. N. Moum (2000), Length scales of turbulence in stably stratified mixing layers, *Phys. Fluids*, *12*(6), 1327-1342, doi:10.1063/1.870385.

Smyth, W. D., and J. N. Moum (2012), Ocean mixing by Kelvin-Helmholtz instability, *Oceanography*, *25*(2), 140-149.

Sottolichio, A., D. Hurther, N. Gratiot, and P. Bretel (2011), Acoustic turbulence measurements of near-bed suspended sediment dynamics in highly turbid waters of a macrotidal estuary, *Cont. Shelf Res.*, *31*(10), S36-S49.

Stillinger, D., K. Helland, and C. Van Atta (1983), Experiments on the transition of homogeneous turbulence to internal waves in a stratified fluid, *J. Fluid Mech.*, *131*, 91-122.

Tang J. H. (2007), Characteristics of fine cohesive sediment’s flocculation in the Changjiang estuary and its adjacent sea area. Master Degree thesis, East China Normal University, May 2007 (in Chinese with English abstract).

Tedford, E., J. Carpenter, R. Pawlowicz, R. Pieters, and G. A. Lawrence (2009), Observation and analysis of shear instability in the Fraser River estuary, *J. Geophys. Res. Oceans*, *114*(C11).

Thomas, D. G. (1963). Non-Newtonian suspensions — part I. physical properties and laminar transport characteristics. *Ind. Eng. Chem. Res.*, 55(11), 18-29.

Thomson, J. (2012), Wave breaking dissipation observed with “SWIFT” drifters, *J. Atmos. Ocean. Technol.*, *29*(12), 1866-1882.

Thorpe, S. (1973), Experiments on the instability and turbulence in a stratified shear flow, *J. Fluid Mech.*, *61*(4), 731-751.

Traykovski, P., Trowbridge, J., & Kineke, G. (2015). Mechanisms of surface wave energy dissipation over a high‐concentration sediment suspension. *J. Geophys. Res. Oceans*, 120(3), 1638-1681.

Trowbridge, J. H., and P. Traykovski (2015), Coupled dynamics of interfacial waves and bed forms in fluid muds over erodible seabeds in oscillatory flows, *J. Geophys. Res. Oceans*, *120*(8), 5698-5709.

Tu, J., D. Fan, Q. Lian, Z. Liu, W. Liu, A. Kaminski, and W. Smyth (2020), Acoustic Observations of Kelvin-Helmholtz Billows on an Estuarine Lutocline, *J. Geophys. Res. Oceans*, *125*(4), e2019JC015383, doi:10.1029/2019jc015383.

Tu, J., D. Fan, Y. Zhang, and G. Voulgaris (2019), Turbulence, Sediment-Induced Stratification, and Mixing Under Macrotidal Estuarine Conditions (Qiantang Estuary, China), *J. Geophys. Res. Oceans*, *124*(6), 4058-4077, doi:10.1029/2018jc014281.

Van Haren, H., and L. Gostiaux (2010), A deep-ocean Kelvin-Helmholtz billow train, *Geophys. Res. Lett.*, *37*(3).

Vinzon, S. B., & Mehta, A. J. (2000). Boundary layer effects due to suspended sediment in the Amazon River Estuary. In W. H. McAnally & A. J. Mehta (Eds.), Proceedings in Marine Science (Vol. 3, pp. 359-372): Elsevier.

Walter, R. K., N. J. Nidzieko, and S. G. Monismith (2011), Similarity scaling of turbulence spectra and cospectra in a shallow tidal flow, *J. Geophys. Res. Oceans*, *116*(C10).

Wang Q. Z. (2021), Rheological study of fine sediment in estuary. Master Degree thesis, East China Normal University, June 2021 (in Chinese with English abstract).

Wang, X. H., and H. Wang (2010), Tidal straining effect on the suspended sediment transport in the Huanghe (Yellow River) Estuary, China, *Ocean Dyn.*, *60*(5), 1273-1283, doi:10.1007/s10236-010-0298-y.

Welch, P. (1967), The use of fast Fourier transform for the estimation of power spectra: a method based on time averaging over short, modified periodograms, *IEEE Transactions on audio and electroacoustics*, 15(2), 70-73.

Wiles, P. J., T. P. Rippeth, J. H. Simpson, and P. J. Hendricks (2006), A novel technique for measuring the rate of turbulent dissipation in the marine environment, *Geophys. Res. Lett.*, *33*(21).

Woods, J. (1969), On Richardson's number as a criterion for laminar-turbulent-laminar transition in the ocean and atmosphere, *Radio Sci.*, 4(12), 1289-1298.

Wright, L., Z.-S. Yang, B. Bornhold, G. Keller, D. Prior, W. Wiseman, Y. Fan, and Z. Su (1986), Short period internal waves over the Huanghe (Yellow River) delta front, *Geo-Mar. Lett.*, *6*(2), 115-120.